



# Construction of Pt/graphitic C<sub>3</sub>N<sub>4</sub>/MoS<sub>2</sub> heterostructures on photo-enhanced electrocatalytic oxidation of small organic molecules

Chunyang Zhai<sup>a,1</sup>, Mingjuan Sun<sup>a,1</sup>, Lixi Zeng<sup>b</sup>, Mianqiang Xue<sup>c</sup>, Jianguo Pan<sup>a</sup>, Yukou Du<sup>d</sup>, Mingshan Zhu<sup>a,b,\*</sup>

<sup>a</sup> School of Materials Science and Chemical Engineering, Ningbo University, Ningbo 315211, PR China

<sup>b</sup> Guangdong Key Laboratory of Environmental Pollution and Health, School of Environment, Jinan University, Guangzhou 510632, PR China

<sup>c</sup> Research Institute of Science for Safety and Sustainability, National Institute of Advanced Industrial Science and Technology, Ibaraki 305-8569, Japan

<sup>d</sup> College of Chemistry, Chemical Engineering and Materials Science, Soochow University, Suzhou 215123, PR China

## ARTICLE INFO

### Keywords:

Photofunctional  
Electrode  
Graphitic carbon nitride  
Molybdenum disulfide  
Visible light  
Fuel cell reaction

## ABSTRACT

Low temperature fuel cells, with the features of clean, environmental friendliness, and high energy density, are considered as ideal future green energy sources. It has been recently demonstrated that the activities and stabilities of traditional fuel cell reactions can be improved by using photo-functional electrodes with assistance of light illumination. Two-dimensional (2D) heterostructure of g-C<sub>3</sub>N<sub>4</sub>/MoS<sub>2</sub> was demonstrated to be a promising photocatalyst. Herein, we used g-C<sub>3</sub>N<sub>4</sub>/MoS<sub>2</sub> nanosheets as a photo-functional substrate for the decoration of Pt nanoparticles and then applied on fuel cell electrocatalytic reactions. Comparing with traditional electrocatalytic reactions, the electrocatalytic performances of the as-synthesized Pt/g-C<sub>3</sub>N<sub>4</sub>/MoS<sub>2</sub> for the oxidation of methanol, ethanol, and formic acid upon visible light illumination are improved with 6.5, 2.2, and 2.5 times, respectively. The decisive factors in the improved catalytic performances are the synergistic effect of photo&electro-process and the effective charge separation in the designed 2D/2D g-C<sub>3</sub>N<sub>4</sub>/MoS<sub>2</sub> heterostructure.

## 1. Introduction

Owing to their low emission of contamination, high-energy density, and ultra-fast recharging, fuel cells have been acted as an alternative power-generation technique to convert chemical energy directly into electrical energy [1–7]. Up to date, various fuel cells such as direct methanol fuel cell (DMFC), direct ethanol fuel cell (DEFC), and direct formic acid fuel cell (DFAFC) have received great interest [1–4]. This is because those small organic molecules (SOMs) including ethanol, methanol, and formic acid have high mass energy density and easy storage and transport. In most cases, platinum (Pt) was used as the most effective electrocatalyst in the electrocatalytic oxidation of liquid fuel (viz. methanol, ethanol, formic acid...) [3–5]. However, due to the easy poisonous by carbonaceous intermediates together with the high cost of Pt, great efforts are still required to address the rapid increasing energy demands.

Accordingly, extensive efforts have been done to develop electrocatalysts supports to improve the performance of electrode. On one hand, the Pt electrocatalysts can be dispersed well on the surfaces of supports, which increases the catalytic active sites. Moreover, such

supports also decrease the usage amount of Pt, contributing to the low-cost of electrodes. On the other hand, these supports have co-catalytic properties such as adsorption ability. Currently, semiconductor materials have been certified as candidates of electrocatalysts carriers. We all have known that these semiconductors are used as photocatalysts and have powerful oxidation ability after light irradiation. Therefore, a novel photo-enhanced fuel cell system was constructed, in which the SOMs could be oxidized by synergistic effect of electro&photo-catalytic process on a metal/semiconductor electrode upon light irradiation [6–16]. With the assistance of light irradiation, the activities and stabilities of traditional fuel cell reaction for SOM oxidation at ambient environment were greatly improved [6,7].

More recently, ultrathin two dimensional (2D) semiconductor material has received considerable attention in the field of artificial photosynthesis because of their origin 2D structural features and optical properties [17–19]. 2D graphite carbon nitride (g-C<sub>3</sub>N<sub>4</sub>) nanosheets have been used for various photocatalytic applications including organic photosynthesis, water contamination treatment and water splitting [19–25]. Nevertheless, because of the rapid recombination of photogenerated charge holes and electrons, the photocatalytic

\* Corresponding author at: School of Materials Science and Chemical Engineering, Ningbo University, Ningbo 315211, PR China.

E-mail address: [mingshanzhu@yahoo.com](mailto:mingshanzhu@yahoo.com) (M. Zhu).

<sup>1</sup> These authors contributed equally to this work.

efficiency of pure g-C<sub>3</sub>N<sub>4</sub> is still far from satisfactory. Accordingly, significant efforts have been made to enhance the charges separation by coupling with the other materials [19,26,20–31]. In general, 2D/2D heterostructures are the most expected owing to the advantages of abundant coupling interfaces and large contact surface, which contribute to the improved photogenerated charges migration and enhanced the photocatalytic activity [19,26,20–31]. It is well recognized that 2D-layered transition metal disulfides (TMDs) such as molybdenum disulfide (MoS<sub>2</sub>) has been considered as promising candidates of co-catalysts to improve the rate of charge separation in recent years [32–34]. Hence, 2D layered MoS<sub>2</sub> was coupled with g-C<sub>3</sub>N<sub>4</sub> to construct 2D/2D heterostructures [35–39]. For example, Majima group showed that the photogenerated electrons from g-C<sub>3</sub>N<sub>4</sub> can be rapid injected to MoS<sub>2</sub>, resulting in enhanced photocatalytic activity on H<sub>2</sub> production [39].

However, the above efforts most focused on the applications of heterostructure of g-C<sub>3</sub>N<sub>4</sub>/MoS<sub>2</sub> on photocatalysis, and there are very few works beyond this category. To further extend the application of g-C<sub>3</sub>N<sub>4</sub>/MoS<sub>2</sub> composite, we used it as a support for the deposition of Pt electrocatalysts to fabricate Pt/g-C<sub>3</sub>N<sub>4</sub>/MoS<sub>2</sub> electrode. The as-prepared composite electrode was used as anode in the investigation of electrocatalytic oxidation of SOMs including methanol, ethanol, and formic acid for the first time. Owing to their nice visible light response, Pt/g-C<sub>3</sub>N<sub>4</sub>/MoS<sub>2</sub> showed obvious enhanced electrocatalytic performance after visible light illumination compared to electrocatalytic process and Pt decorated single-component *viz.* Pt/g-C<sub>3</sub>N<sub>4</sub> and Pt/MoS<sub>2</sub> composites under visible light illumination. Efficient interfacial charger carrier mobility is observed in the desired 2D/2D heterostructures contributing to the great improvement of electrocatalytic activities under visible light illumination. The present results display that the construction of 2D/2D heterostructures opens new opportunity in the application of fuel cell reactions.

## 2. Experimental

### 2.1. Chemicals

Urea [CO(NH<sub>2</sub>)<sub>2</sub>, AR, CAS 57-13-6], chloroplatinic acid hexahydrate (H<sub>2</sub>PtCl<sub>6</sub>·6H<sub>2</sub>O, AR, CAS 18497-13-7), ammonium tetrathiomolybdate [(NH<sub>4</sub>)<sub>2</sub>MoS<sub>4</sub>, AR, CAS 15060-55-6], dimethyl formamide (DMF, AR, CAS 68-12-2), sulphuric acid (H<sub>2</sub>SO<sub>4</sub>, AR, CAS 7664-93-9), potassium hydroxide (KOH, AR, CAS 1310-58-3), ethanol (CH<sub>3</sub>CH<sub>2</sub>OH, EtOH, AR, CAS 64-17-5), methanol (CH<sub>3</sub>OH, MeOH, AR, CAS 67-56-1), and formic acid (HCOOH, AR, CAS 64-18-8) were purchased (Sinopharm Chemical, China) and were used directly without any purification.

### 2.2. Synthesis of g-C<sub>3</sub>N<sub>4</sub>, MoS<sub>2</sub>, and heterostructure of g-C<sub>3</sub>N<sub>4</sub>/MoS<sub>2</sub>

The nanosheets of g-C<sub>3</sub>N<sub>4</sub> were obtained through heating the urea in the semi-closed environment [40]. In a typical experiment, urea powders (10 g) were dissolved into water (15 mL). The pH of above solution was adjusted to 4–5 by HCl and then dried at 80 °C with 12 h. The samples were put into an alumina crucible with a lid. The crucible was then put in the muffle furnace and held at 550 °C for 2 h with the heating rate of 5 °C min<sup>−1</sup>.

The g-C<sub>3</sub>N<sub>4</sub>/MoS<sub>2</sub> was synthesized via a solvothermal method. 0.09 g g-C<sub>3</sub>N<sub>4</sub> and 0.008 g ammonium tetrathiomolybdate were dispersed into 15 ml DMF under 20 min ultrasonication, and then transferred into Teflon autoclave (V: 25 mL). The above autoclave was held at 200 °C for 12 h. The powders were obtained through centrifugation and then washed by ethanol completely, and dried at 70 °C in an oven, obtaining the heterostructure of g-C<sub>3</sub>N<sub>4</sub>/MoS<sub>2</sub>. The weight ratio of MoS<sub>2</sub> in the g-C<sub>3</sub>N<sub>4</sub>/MoS<sub>2</sub> is about 10 wt%. The different ratios of MoS<sub>2</sub> in g-C<sub>3</sub>N<sub>4</sub>/MoS<sub>2</sub> were synthesized through using different amounts of ammonium tetrathiomolybdate. The pure MoS<sub>2</sub> were prepared with same method without ammonium tetrathiomolybdate g-C<sub>3</sub>N<sub>4</sub>.

### 2.3. Preparation of Pt/g-C<sub>3</sub>N<sub>4</sub>, Pt/MoS<sub>2</sub>, and Pt/g-C<sub>3</sub>N<sub>4</sub>/MoS<sub>2</sub>

The Pt/g-C<sub>3</sub>N<sub>4</sub>/MoS<sub>2</sub> nanocomposite was prepared via a hydrothermal approach. 20 mg g-C<sub>3</sub>N<sub>4</sub>/MoS<sub>2</sub> and 0.68 ml H<sub>2</sub>PtCl<sub>6</sub> aqueous solution (3.9 × 10<sup>−2</sup> M) were dispersed into ethanol-H<sub>2</sub>O mixtures (20 mL, vol = 1:1) under ultrasonication for 30 min. The mixtures were then transferred into Teflon autoclave (V: 25 mL). The above autoclave was held at 140 °C for 4 h and cooled down naturally. The powders were obtained via centrifugation and then washed by ethanol thoroughly and dried at 70 °C in an oven, obtaining the Pt/g-C<sub>3</sub>N<sub>4</sub>/MoS<sub>2</sub>. The weight ratio of Pt is *ca.* 20 wt% for total mass. The Pt/g-C<sub>3</sub>N<sub>4</sub> and Pt/MoS<sub>2</sub> were prepared with similar method that the g-C<sub>3</sub>N<sub>4</sub>/MoS<sub>2</sub> was replaced by bare C<sub>3</sub>N<sub>4</sub> and MoS<sub>2</sub>, respectively.

### 2.4. Preparation of Pt/g-C<sub>3</sub>N<sub>4</sub>/MoS<sub>2</sub>, Pt/MoS<sub>2</sub>, Pt/g-C<sub>3</sub>N<sub>4</sub> modified electrodes

The Pt/g-C<sub>3</sub>N<sub>4</sub>/MoS<sub>2</sub> electrode was prepared through coating the Pt/g-C<sub>3</sub>N<sub>4</sub>/MoS<sub>2</sub> on a 3 mm in diameter of L-type glassy carbon electrode (GCE). Typically, Pt/g-C<sub>3</sub>N<sub>4</sub>/MoS<sub>2</sub> (2 mg) and Nafion solutions (5 wt%, 10 μL) were added into ethanol-H<sub>2</sub>O mixtures (1 mL, vol = 1:1) with 30 min ultrasonication to get the dispersion homogeneously. After, 5 μL of the above dispersion was dispersed onto the surface of L-type GCE and dried at the ambient condition (containing 2 μg of Pt). The Pt/g-C<sub>3</sub>N<sub>4</sub> and Pt/MoS<sub>2</sub> electrodes were prepared with same method, in which Pt/g-C<sub>3</sub>N<sub>4</sub> and Pt/MoS<sub>2</sub> were used, respectively.

### 2.5. Photoelectrocatalytic measurements

The photoelectrocatalytic measurements were employed on a quartz reactor with an electrochemical workstation (CHI 660E), in which modified GCE, Pt wire, and Ag/AgCl were acted as working electrode, counter electrode, and reference electrode, respectively. The photoelectrocatalytic activity of methanol, ethanol, and formic acid was carried out by cyclic voltammetry (CV) measurements. The scan rate is 50 mV s<sup>−1</sup>. Chronoamperometries (CA) of samples under visible light illumination or dark condition were measured at −0.2 V in 1 M EtOH + 1 M KOH solution. The chronopotentiometric curves of Pt/g-C<sub>3</sub>N<sub>4</sub>/MoS<sub>2</sub> electrode were carried out at 100 μA under dark condition and visible light illumination. The photocurrent responses were measured in 0.1 M aqueous solution of Na<sub>2</sub>SO<sub>4</sub> at 0.6 V. The electrochemical impedance spectroscopy (EIS) was measured in 1 M EtOH + 1 M KOH, 1 M MeOH + 1 M KOH, 0.5 M HCOOH + 0.5 M H<sub>2</sub>SO<sub>4</sub> and 0.1 M Na<sub>2</sub>SO<sub>4</sub>, respectively. The EIS at different potentials were measured in 1 M EtOH + 1 M KOH solution over the frequency range between 0.1 and 10<sup>5</sup> Hz under an AC voltage amplitude of 5.0 mV.

During photoelectrocatalytic measurements, a xenon lamp (500 W) was used as light source and a 420 nm long pass filter was put before reactor.

### 2.6. Characterization

Transmission electron microscopy (TEM, JEOL-2100, operated at 120 kV, HAADF-STEM image and corresponding EDX elemental mapping operated at 200 kV) was used to evaluate the morphology and component of samples. X-ray photoelectron spectroscopy (XPS, JEOL JPS-9010 MC spectrometer) and X-ray diffraction (XRD, BrukerD8Focus, with Cu Kα radiation (50 kV) of wavelength λ = 1.5418 Å) were investigated to the component and phase structures of samples, respectively. The UV–vis properties of samples were carried out by using a UV–vis-NIR Spectrophotometer on LAMBDA 950 UV/Vis/NIR Spectrophotometer. The photoluminescence (PL) properties of samples were carried out by using fluorospectrophotometer (Edinburgh FLS920) with the excitation wavelength at 405 nm.

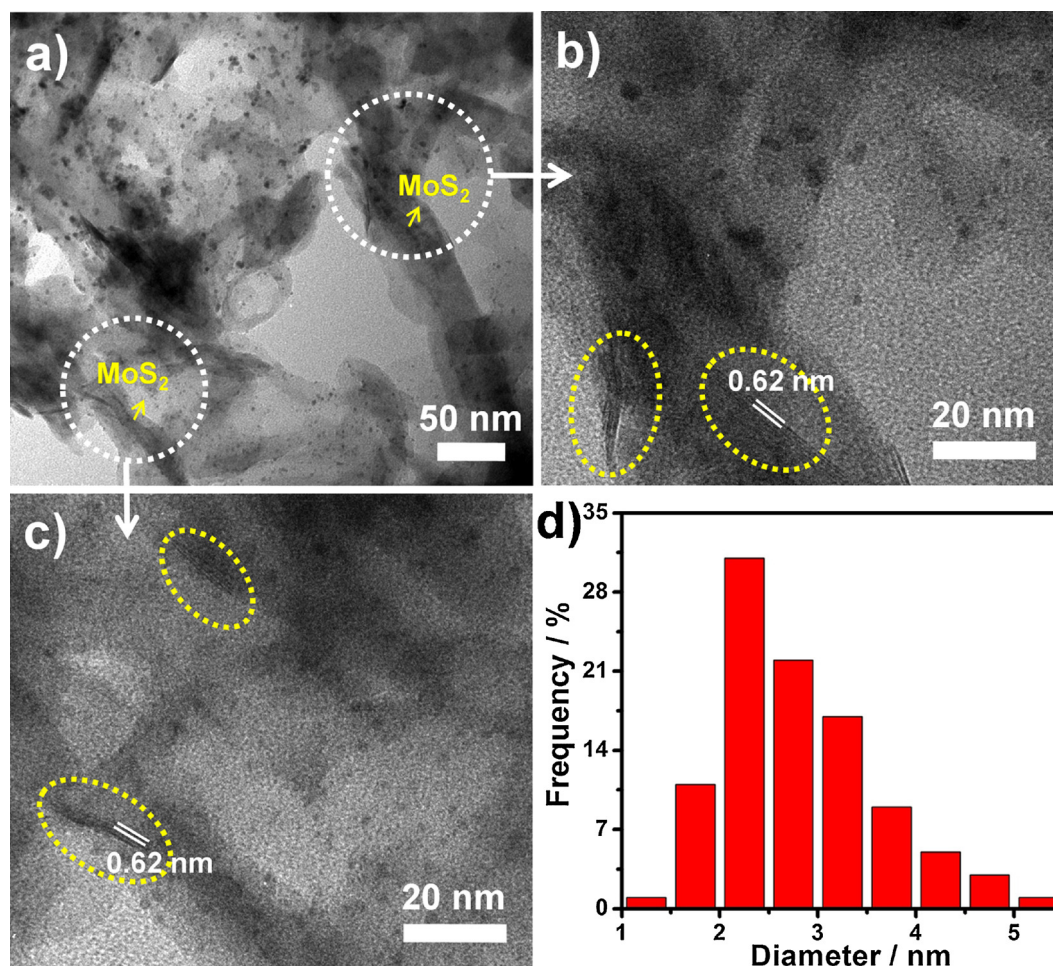


**Fig. 1.** TEM (a) and HRTEM (b, c) images of Pt/g-C<sub>3</sub>N<sub>4</sub>/MoS<sub>2</sub> nanocomposites. Particle size distribution histogram (d) of Pt nanoparticles on g-C<sub>3</sub>N<sub>4</sub>/MoS<sub>2</sub> from Fig. 1c and b.

### 3. Results and discussion

#### 3.1. Characterization of g-C<sub>3</sub>N<sub>4</sub>, MoS<sub>2</sub>, and g-C<sub>3</sub>N<sub>4</sub>/MoS<sub>2</sub> and Pt/g-C<sub>3</sub>N<sub>4</sub>/MoS<sub>2</sub>

The 2D morphologies of g-C<sub>3</sub>N<sub>4</sub>, MoS<sub>2</sub>, and g-C<sub>3</sub>N<sub>4</sub>/MoS<sub>2</sub> nanosheets were demonstrated by TEM. Figs. S1a and S1b show the pure g-C<sub>3</sub>N<sub>4</sub> and MoS<sub>2</sub> with a sheet-like morphology and size range from 200 nm to 1  $\mu$ m and 50 to 200 nm, respectively. After hybridized with MoS<sub>2</sub>, small sized of MoS<sub>2</sub> nanosheets attached on the surface of g-C<sub>3</sub>N<sub>4</sub> can be easily observed, as shown in Fig. S1c. In general, 2D sheet-like materials can be used as promising supports for the growth of metal nanoparticles. Fig. 1a shows that small nanoparticles of Pt were well decorated on the surface of g-C<sub>3</sub>N<sub>4</sub>/MoS<sub>2</sub> nanocomposites. To clear show the size of Pt nanoparticles and fine structure of MoS<sub>2</sub>, HRTEM images of Pt/g-C<sub>3</sub>N<sub>4</sub>/MoS<sub>2</sub> from two different dotted circles in the Fig. 1a were displayed in Fig. 1b and c. Beside small particles of Pt, lattice fringes (d-spacing: 0.62 nm) were easily detected, which attributed to (002) plane of MoS<sub>2</sub>. The average diameter of Pt decorated on g-C<sub>3</sub>N<sub>4</sub>/MoS<sub>2</sub> nanosheets is ca. 3.0 nm, as shown in Fig. 1d. Furthermore, the pure g-C<sub>3</sub>N<sub>4</sub> and MoS<sub>2</sub> nanosheets were also used as the substrates to deposit Pt nanoparticles, respectively. As shown in Fig. S2, similar sizes of Pt nanoparticles were observed in Pt/g-C<sub>3</sub>N<sub>4</sub> and Pt/MoS<sub>2</sub> composites.

The HAADF-STEM image, EDX spectra, and EDX elemental mapping of Pt/g-C<sub>3</sub>N<sub>4</sub>/MoS<sub>2</sub> were provided to investigate the composition and the distribution of different elements on the surface of 2D structures. In the Fig. 2a, lots of bright dots which are Pt nanoparticles, were well

dispersed on the surface of g-C<sub>3</sub>N<sub>4</sub> sheets. Beside the nanosheets and bright dots, a piece of bright sheet was also detected on g-C<sub>3</sub>N<sub>4</sub> sheets surface, which might be MoS<sub>2</sub>. To confirm these conclusions, EDX at the selected zones were collected. It can be seen that the C, N, Pt, Mo, and S elements were easily detected in the Fig. 2b, while only C, N and Pt elements were found in the Fig. 2c. To further demonstrate the above phenomena, the EDX element mapping with different elements were provided, which the different components of g-C<sub>3</sub>N<sub>4</sub>, MoS<sub>2</sub> and Pt were easily observed. These results clearly show that the Pt and MoS<sub>2</sub> were hybridized with 2D g-C<sub>3</sub>N<sub>4</sub> sheets.

To identify the elements and interaction of as-prepared samples, the X-ray photoelectron spectroscopy (XPS) of bare g-C<sub>3</sub>N<sub>4</sub>, MoS<sub>2</sub>, and g-C<sub>3</sub>N<sub>4</sub>/MoS<sub>2</sub> were investigated (Fig. 3). Firstly, three peaks at 398.7, 400.2, and 401.4 eV were observed in pure g-C<sub>3</sub>N<sub>4</sub>, which are corresponded to C–N, tertiary nitrogen N–C3, and C–N–H groups, respectively [28,41]. Secondly, for pure MoS<sub>2</sub>, two characteristic peaks corresponding to S 2p<sub>1/2</sub> and S 2p<sub>3/2</sub>, and Mo 3d<sub>3/2</sub> and Mo 3d<sub>5/2</sub>, are observed at ca. 163.2 and 162.0 eV, and 232.1 and 229.0 eV, respectively [27,42]. Interestingly, the binding energies of N 1s, S 2p, and Mo 3d were slightly shifted in the g-C<sub>3</sub>N<sub>4</sub>/MoS<sub>2</sub>, in which the binding energies of N 1s shift to the higher binding energies while those of S 2p and Mo 3d shift to the lower binding energies, respectively. These binding energy shifts in the composites is due to the interaction of two components [41]. In the Pt/g-C<sub>3</sub>N<sub>4</sub>/MoS<sub>2</sub>, beside the above elements, two peaks assigning to Pt 4f<sub>7/2</sub> and Pt 4f<sub>5/2</sub> were easily observed, in which at 72.0 and 75.2 eV, respectively (Fig. S3). The corresponding values are matched well with Pt (0), indicating metallic Pt nanoparticles in Pt/g-C<sub>3</sub>N<sub>4</sub>/MoS<sub>2</sub> [10,42].



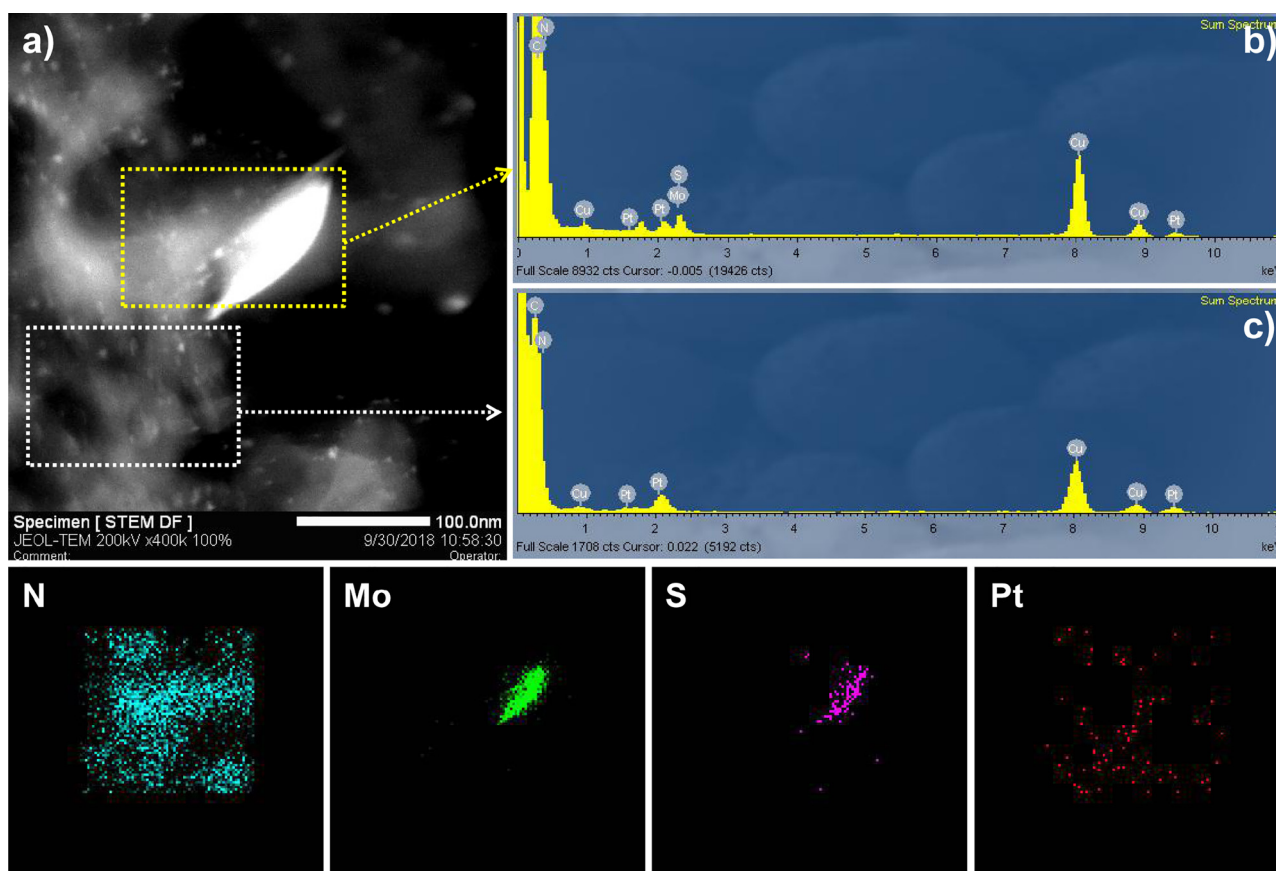


Fig. 2. HAADF-STEM image (a), EDX spectra of different areas (b and c), and element mapping of N, Mo, S, and Pt elements of Pt/g-C<sub>3</sub>N<sub>4</sub>/MoS<sub>2</sub>.

XRD patterns of the as-prepared samples were measured to characterize the crystalline phases, and the results were reflected in Fig. 4A. It can be seen that all g-C<sub>3</sub>N<sub>4</sub> based samples show one main characteristic peak at 27.4°, which contributes to the diffraction of (002) plane for g-C<sub>3</sub>N<sub>4</sub> nanosheets [27]. For pure MoS<sub>2</sub>, two characteristic peaks at ca. 32.7° and 56.7° were observed, which are contributed to the (100) and (110) crystal planes of MoS<sub>2</sub> (JCPDS No. 37-1492) [27]. In the composite of g-C<sub>3</sub>N<sub>4</sub>/MoS<sub>2</sub>, the diffraction peaks of the MoS<sub>2</sub> in the g-C<sub>3</sub>N<sub>4</sub>/MoS<sub>2</sub> nanocomposites can not be observed easily, due to the low weight content of MoS<sub>2</sub> (5 wt%). The similar result has been reported previously by others [27]. However, when the weight content of MoS<sub>2</sub> is increased to 20 wt%, two small peaks can be observed at 32.7° and 56.7°, indicating the formation of g-C<sub>3</sub>N<sub>4</sub>/MoS<sub>2</sub> nanocomposites. To Pt/g-C<sub>3</sub>N<sub>4</sub>/MoS<sub>2</sub>, beside the above peaks, three different peaks at ca. 39.7°, 46.2°, and 67.9° were detected in Pt/g-C<sub>3</sub>N<sub>4</sub>/MoS<sub>2</sub>. These peaks are assigned to the (111), (200), and (220) planes of Pt [43], which further indicate the formation of metallic Pt in the composites of Pt/g-

C<sub>3</sub>N<sub>4</sub>/MoS<sub>2</sub>.

The optical properties of the g-C<sub>3</sub>N<sub>4</sub>, MoS<sub>2</sub>, g-C<sub>3</sub>N<sub>4</sub>/MoS<sub>2</sub> and Pt/g-C<sub>3</sub>N<sub>4</sub>/MoS<sub>2</sub> were investigated by using the UV-vis diffuse reflectance spectra (UV-vis DRS). Fig. 4B shows the pure g-C<sub>3</sub>N<sub>4</sub> with an absorption edge at around 452 nm, indicating that the as-prepared g-C<sub>3</sub>N<sub>4</sub> has 2.7 eV band gap. Pure MoS<sub>2</sub> showed a broad absorption in the visible region owing to the narrow band gap. When the different MoS<sub>2</sub> were hybridized with g-C<sub>3</sub>N<sub>4</sub> nanosheets, tailed absorptions in the far visible region were observed in the presence of MoS<sub>2</sub>. Similar phenomena were observed in the other reports [27,29]. When Pt nanoparticles were loaded on the surface of g-C<sub>3</sub>N<sub>4</sub>/MoS<sub>2</sub>, beside the absorption of g-C<sub>3</sub>N<sub>4</sub> and MoS<sub>2</sub>, an enhanced absorption was observed in the visible region due to the dark color of Pt. These visible light responses in the Pt/g-C<sub>3</sub>N<sub>4</sub>/MoS<sub>2</sub> indicate the potential advantages on photoelectrocatalytic small organic molecules under visible light illumination.

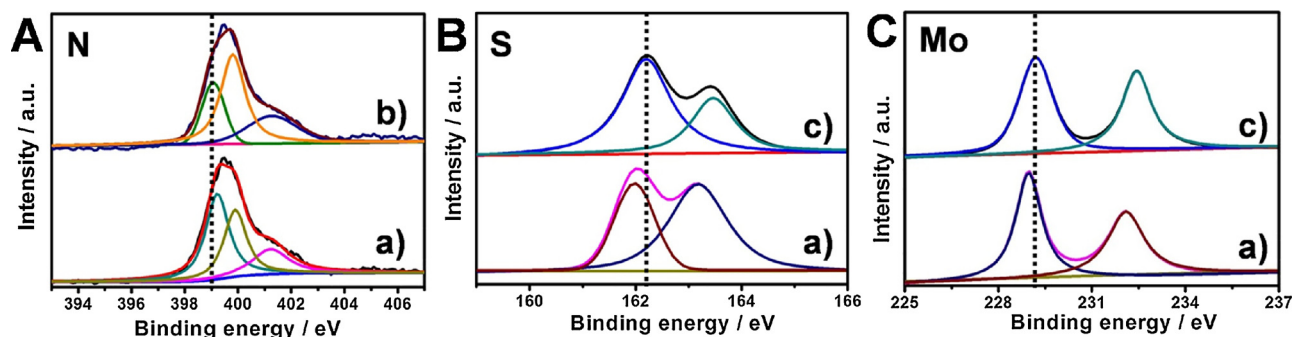


Fig. 3. XPS spectra of N 1s (A), S 2p (B), and Mo 3d (C) of the g-C<sub>3</sub>N<sub>4</sub>/MoS<sub>2</sub> (a), g-C<sub>3</sub>N<sub>4</sub> (b), and MoS<sub>2</sub> (c).

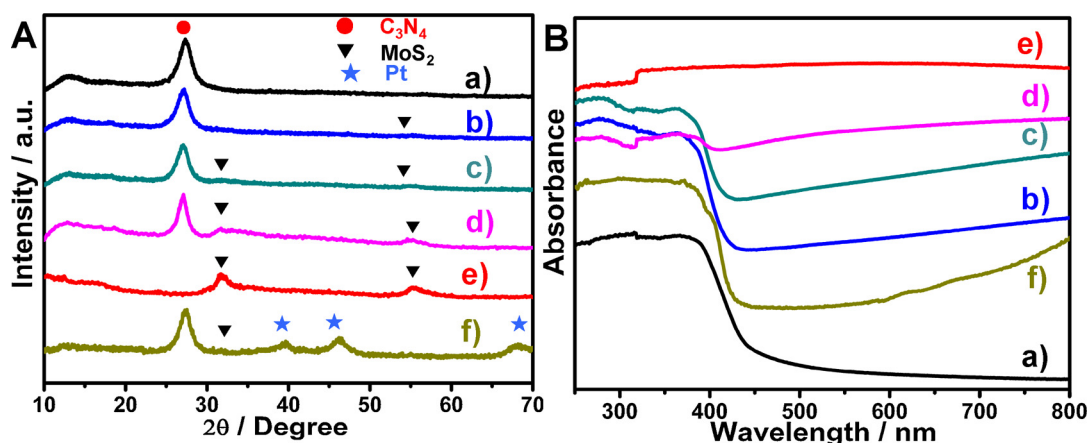


Fig. 4. XRD patterns (A) and UV-vis DRS (B) of  $g-C_3N_4$  (a),  $g-C_3N_4/MoS_2$  5 wt% (b),  $g-C_3N_4/MoS_2$  10 wt% (c),  $g-C_3N_4/MoS_2$  20 wt% (d), pure  $MoS_2$  (e) and Pt/ $g-C_3N_4/MoS_2$  (f).

### 3.2. Oxidation of ethanol on the Pt/ $g-C_3N_4/MoS_2$ catalyst

The electrocatalytic and photoelectrocatalytic properties of the as-obtained electrodes were evaluated through catalytic oxidation of SOMs including methanol, ethanol, and formic acid, respectively. Fig. 5A shows the cyclic voltammeteries (CVs) curves at the potential range from -0.9 to 0.2 V by using Pt/ $g-C_3N_4$  and Pt/ $g-C_3N_4/MoS_2$  as working electrodes for the electrocatalytic ethanol oxidation. There are two characteristic oxidation peaks observed at around -0.2 V in forward curve and -0.3 V in backward curve. The current density of forward peak for Pt/ $g-C_3N_4$  is about  $10.9 \text{ mA mg}^{-1}_{Pt}$ . When the 10 wt% of  $MoS_2$  was hybridized with  $C_3N_4$  nanosheets, the peak current density was improved to  $76.9 \text{ mA mg}^{-1}_{Pt}$ . As comparison, the pure GCE,  $g-C_3N_4$  and  $MoS_2$  modified electrodes for the oxidation of EtOH displayed negligible catalytic activities (Fig. S4).

Owing to the excellent photocatalytic property of  $g-C_3N_4$ , the corresponding Pt/ $g-C_3N_4$  and Pt/ $g-C_3N_4/MoS_2$  electrodes were used upon visible light illumination for the oxidation of ethanol under the same conditions. As expected, the forward peak current densities of both electrodes were improved. The corresponding peak current densities were summarized in Table 1. Comparing with Pt/ $g-C_3N_4$ , the Pt/ $g-C_3N_4/MoS_2$  was more effective towards ethanol oxidation under visible light irradiation. These results suggest that the layered  $MoS_2$  plays a crucial role in the improvement of the electrocatalytic performance. The effects of  $MoS_2$  ratio in Pt/ $g-C_3N_4/MoS_2$  for photoelectrocatalytic oxidation of ethanol were measured under dark environment and visible light illumination. Fig. 5B shows that the optimum loading of  $MoS_2$  in Pt/ $g-C_3N_4/MoS_2$  was 10 wt%, in which the forward peak current

densities reached  $165.5 \text{ mA mg}^{-1}_{Pt}$  under visible light illumination. Accordingly, the as-prepared Pt/ $g-C_3N_4/MoS_2$  with 10 wt% of  $MoS_2$  was used in the following experiments.

### 3.3. Photoelectrochemical properties of ethanol oxidation

To reveal the catalytic oxidation process of ethanol, the EIS in 1 M EtOH + 1 M KOH solution of as-prepared Pt/ $g-C_3N_4/MoS_2$  under visible light irradiation were studied at different potential (Fig. 6). From -0.55 V to -0.25 V, the diameter of semicircle arc (DSA) was decreased with increasing potentials. In general, when the potential is below the oxidation potential (ca. -0.2 V), the active sites for the oxidation of ethanol are increased because of the removal of intermediate species. These intermediate species are formed from ethanol dehydrogenation at lower potential [40,44]. When the potential is above oxidation potential, the DSA was increased owing to the catalyst surface poisoning by intermediate species. Nevertheless, the arc turned to the second quadrant at -0.15 V (Fig. 6B). This is because of the removal of intermediate species from catalyst surface. Continue to increase the potentials to 0 V, the arc is gradually transferred to positive behavior (Fig. 6C), since the intermediate species were absent [40,44].

To confirm the photo-assisted electrocatalytic process on Pt/ $g-C_3N_4/MoS_2$ , different scan rates on the photoelectrocatalytic oxidation of ethanol with and without visible light illumination were carried out (Fig. 7). Firstly, the peak current densities of electrode were increased with the scan rates increase. Fig. 7B and D show a linear relation between the peak current density ( $i_p$ ) and square root of scan rate ( $v^{1/2}$ ) under dark condition and visible light illumination. The diffusion

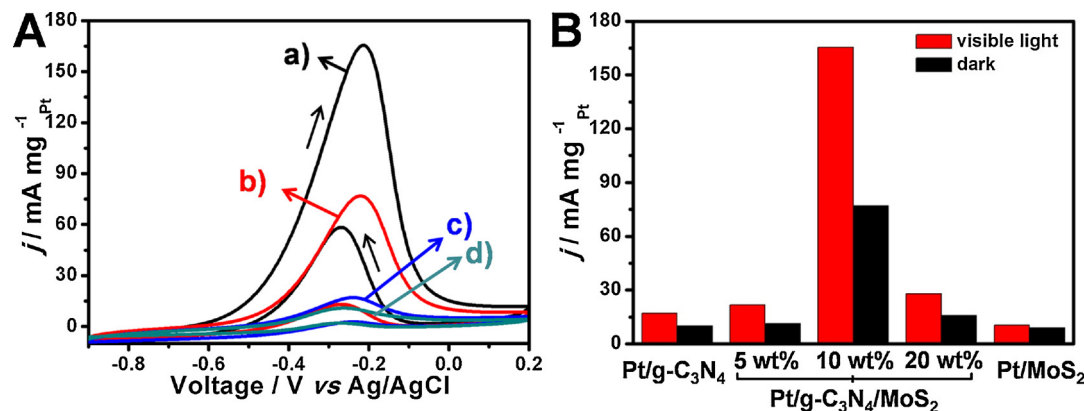


Fig. 5. A: CVs curves of Pt/ $g-C_3N_4/MoS_2$  (a and b) and Pt/ $g-C_3N_4$  (c and d) in 1 M EtOH + 1 M KOH solution with (a and c) and without (b and d) visible light illumination. B: Different electrodes for the oxidation of EtOH under visible light and dark environment.

**Table 1**

The forward peak current densities on different electrodes under visible light illumination and dark environment.

Catalyst	Pt/g-C <sub>3</sub> N <sub>4</sub> (mA mg <sup>-1</sup> Pt)				Pt/MoS <sub>2</sub> (mA mg <sup>-1</sup> Pt)				Pt/g-C <sub>3</sub> N <sub>4</sub> /MoS <sub>2</sub> (mA mg <sup>-1</sup> Pt)			
	Visible light		Dark		Visible light		Dark		Visible light		Dark	
	<i>j</i>	Error	<i>j</i>	Error	<i>j</i>	Error	<i>j</i>	Error	<i>j</i>	Error	<i>j</i>	Error
Methanol	163.1	± 1.5%	97.3	± 1.1%	441.7	± 0.9%	190.8	± 3.4%	1618	± 2.2%	250.5	± 4.5%
Ethanol	17.5	± 4.4%	10.9	± 2.6%	10.5	± 3.5%	6.07	± 4.4%	165.5	± 1.0%	76.9	± 2.3%
Formic acid	281.3	± 1.9%	182.8	± 2.1%	193.7	± 2.2%	50.3	± 4.1%	1557	± 0.3%	624	± 1.7%

coefficient (*D*) of electrode is calculated by Eq. (1):

$$\frac{D_{\text{light}}}{D_{\text{dark}}} = \left[ \frac{\left( \frac{i_p}{v^{1/2}} \right)_{\text{light}}}{\left( \frac{i_p}{v^{1/2}} \right)_{\text{dark}}} \right]^2 \quad (1)$$

From Eq. (1), the value of  $D_{\text{light}}/D_{\text{dark}}$  is 2.7, which indicates the improved electron transfer kinetics at the surface of Pt/g-C<sub>3</sub>N<sub>4</sub>/MoS<sub>2</sub> and thereby contributes to the higher catalytic activity under visible light irradiation [45,46].

In general, the effective interfacial charge transfer between two components contributes to an enhanced photocatalytic performance in the composites. To investigate the photoelectric properties of Pt/g-C<sub>3</sub>N<sub>4</sub>/MoS<sub>2</sub> electrode in 1 M EtOH + 1 M KOH media, the electrochemical impedance spectrum (EIS) and linear sweep voltammetry (LSV) of Pt/g-C<sub>3</sub>N<sub>4</sub> and Pt/g-C<sub>3</sub>N<sub>4</sub>/MoS<sub>2</sub> were carried out. Fig. 8A shows that the DSA of Pt/g-C<sub>3</sub>N<sub>4</sub> is larger than Pt/g-C<sub>3</sub>N<sub>4</sub>/MoS<sub>2</sub>. Moreover, upon visible light irradiation, both of DSAs turned to smaller than those under dark condition. Usually, the smaller DSA means smaller impedance between catalysts and electrolyte and faster interfacial charge transfer on the electrode. These results suggest the decreased internal resistances and facilitated charge transfer in the composites of Pt/g-C<sub>3</sub>N<sub>4</sub>/MoS<sub>2</sub> and those electrodes upon light illumination [47–59].

In addition, the LSV behaviors of above electrodes in the same electrolyte were also investigated with and without visible light irradiation. Fig. 8B shows that the onset potentials on the Pt/g-C<sub>3</sub>N<sub>4</sub>/MoS<sub>2</sub> and Pt/g-C<sub>3</sub>N<sub>4</sub> electrodes under visible light illumination were negatively shifted by comparing with those electrodes under dark condition. The current densities of Pt/g-C<sub>3</sub>N<sub>4</sub>/MoS<sub>2</sub> and Pt/g-C<sub>3</sub>N<sub>4</sub> electrode were 122 and 17.5 mA mg<sup>-1</sup> under visible light illumination at potential of -0.3 V, which are 2.7 and 1.9 times higher than the corresponding electrodes under dark condition, respectively. These enhanced current densities are due to the improved charge mobility in the composites of g-C<sub>3</sub>N<sub>4</sub>/MoS<sub>2</sub> under light excitation.

### 3.4. Oxidation of methanol and formic acid on Pt/g-C<sub>3</sub>N<sub>4</sub>/MoS<sub>2</sub> catalyst

To further prove the Pt-C<sub>3</sub>N<sub>4</sub>/MoS<sub>2</sub> can be acted as a promising

electrocatalyst towards small organic molecules under visible light illumination, methanol and formic acid were also investigated. The CVs for the electrocatalytic oxidation of methanol and formic acid were shown in Fig. 9 and the forward peak current densities of Pt-C<sub>3</sub>N<sub>4</sub>/MoS<sub>2</sub> in different substrates solutions were summarized in Table 1. Compare to dark condition, the peak current densities of electrode were improved 6.5 and 2.5 times in the photoelectrocatalytic oxidation of methanol and formic acid, respectively. The error was below 5% in all our experiments also can be observed.

### 3.5. Photoelectrochemical properties of methanol and formic acid oxidation

Similar to catalytic oxidation of ethanol, the EIS and LSV behaviors of the as-synthesized Pt/g-C<sub>3</sub>N<sub>4</sub>/MoS<sub>2</sub> electrode is also investigated in methanol and formic acid media under visible light illumination and dark environment to further reveal the advantages of light photo-illuminated process. Fig. 10A and C show that the DSAs of Pt/g-C<sub>3</sub>N<sub>4</sub>/MoS<sub>2</sub> electrodes under visible light illumination are much smaller than those under dark condition both in methanol and formic acid system. On the other hand, the LSV behaviors of electrodes demonstrated similar tendencies, which showed the onset potentials were negatively shift and the current densities were enhanced. Furthermore, different scan rates on the photoelectrocatalytic oxidation of methanol and formic acid under visible light and dark environment were investigated (Figs. S5 and S6). The diffusion coefficients ( $D_{\text{light}}/D_{\text{dark}}$ ) for methanol and formic acid are 27.6 and 5.7, respectively.

### 3.6. Stability of Pt/g-C<sub>3</sub>N<sub>4</sub>/MoS<sub>2</sub> catalyst

The long-term stability of electrocatalyst is a crucial parameter in fuel cells. Fig. 11A shows the chronoamperometric curves of the as-synthesized Pt/g-C<sub>3</sub>N<sub>4</sub>/MoS<sub>2</sub> within 3000 s both under dark environment and visible light illumination. The electrode shows stable electrocatalytic performance in both conditions, while the current density was higher under visible light illumination than that of under dark environment, revealing superior catalytic activity in photo-illuminated process. In the chronopotentiometry spectra, the potential is gradually increased with the polarization time, indicating a better catalyst's poisoning resistance. The catalyst turns to be poisoned when the voltage

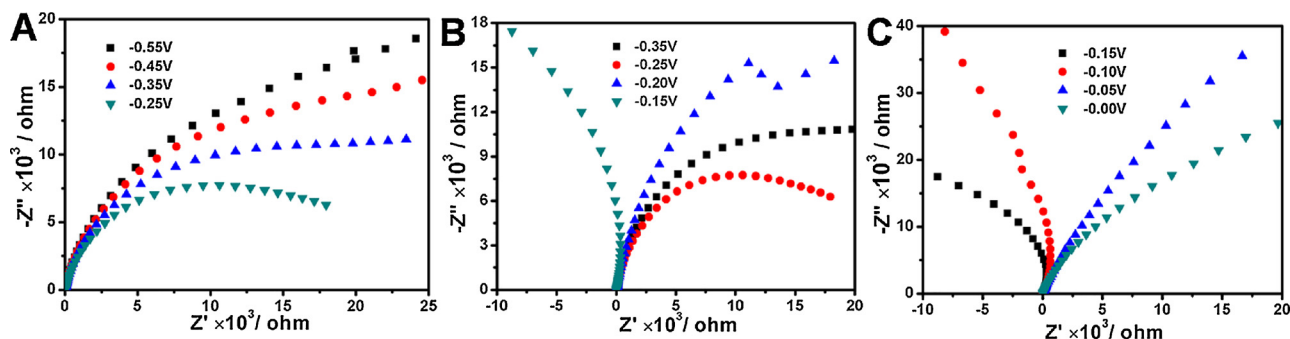


Fig. 6. EIS spectra of Pt/g-C<sub>3</sub>N<sub>4</sub>/MoS<sub>2</sub> electrode at different potentials in 1 M EtOH + 1 M KOH solution under visible light irradiation.

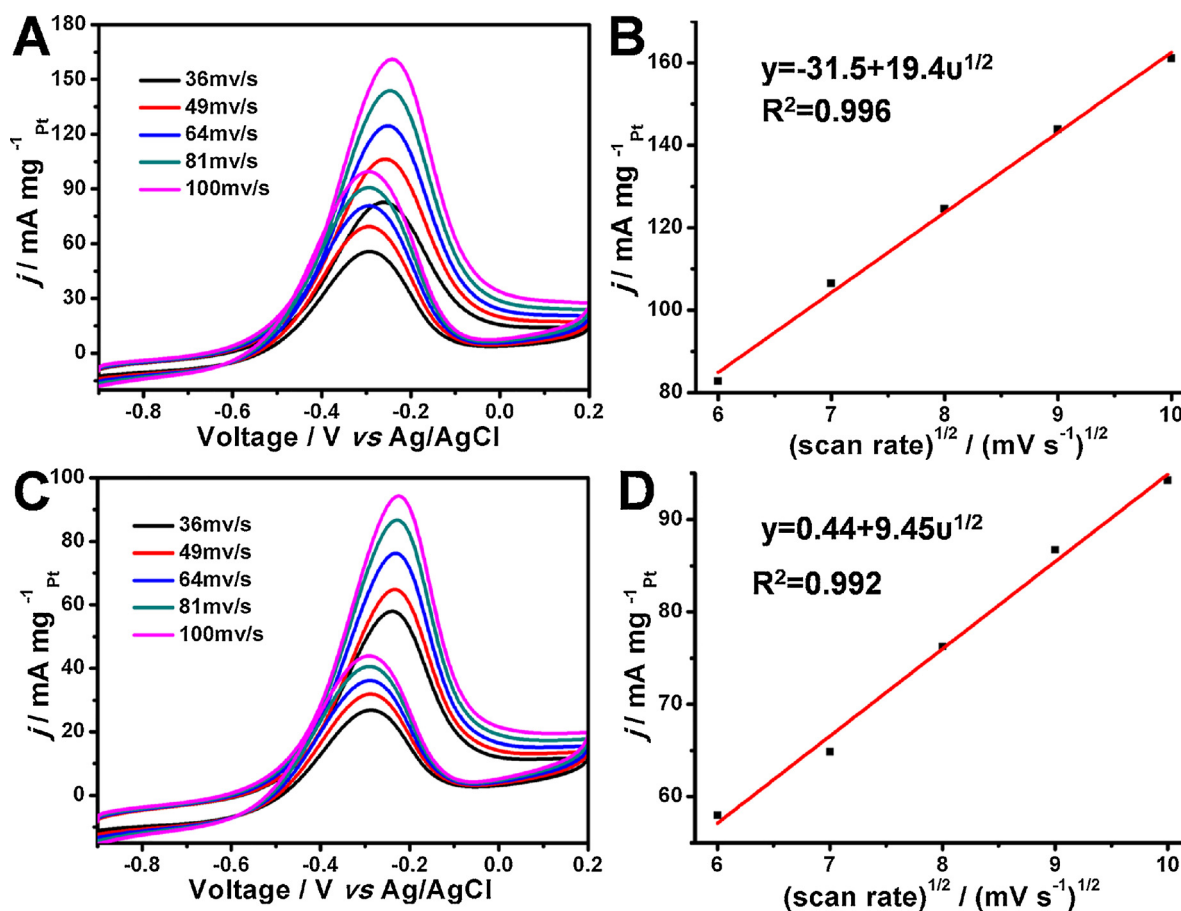


Fig. 7. A and C: CVs of Pt/g-C<sub>3</sub>N<sub>4</sub>/MoS<sub>2</sub> at different scan rate in 1 M EtOH + 1 M KOH solution. B and D: The dependence of  $i_p$  on the  $v^{1/2}$ . The electrode was irradiated by visible light (A and B) and under dark (C and D) condition.

increased rapidly [50]. Fig. 11B suggests the chronopotentiometry spectra of electrode both under dark condition and visible light illumination. When the electrode is upon irradiated by visible light, the potential of Pt/g-C<sub>3</sub>N<sub>4</sub>/MoS<sub>2</sub> electrode jumped to a much higher potential after 14,600 s, which is ca. 41.5 times than that of under dark environment (352 s). This result indicates Pt/g-C<sub>3</sub>N<sub>4</sub>/MoS<sub>2</sub> electrode has the better anti-poisoning ability under visible light illumination, which contributes to the higher catalytic activity. Although these intermediate carbonaceous species can be partial removed by the strong oxidative ability of radical ions, the catalysts still need to bear the intermediate carbonaceous species, which poisoned the catalyst after

long-time catalytic process. It still has a long way to get a successful real application.

### 3.7. Photoelectrochemical properties of Pt/g-C<sub>3</sub>N<sub>4</sub>/MoS<sub>2</sub> catalyst

Above results solidly demonstrated that the as-prepared Pt/g-C<sub>3</sub>N<sub>4</sub>/MoS<sub>2</sub> electrode is an efficient photoelectrocatalyst for the oxidation of small organic molecules with assistance of visible light irradiation. In general, the photocatalytic activity is highly depending on the ratio of the photogenerated charge separation. On the other hand, in comparison with the other structures, 2D/2D heterostructures possess

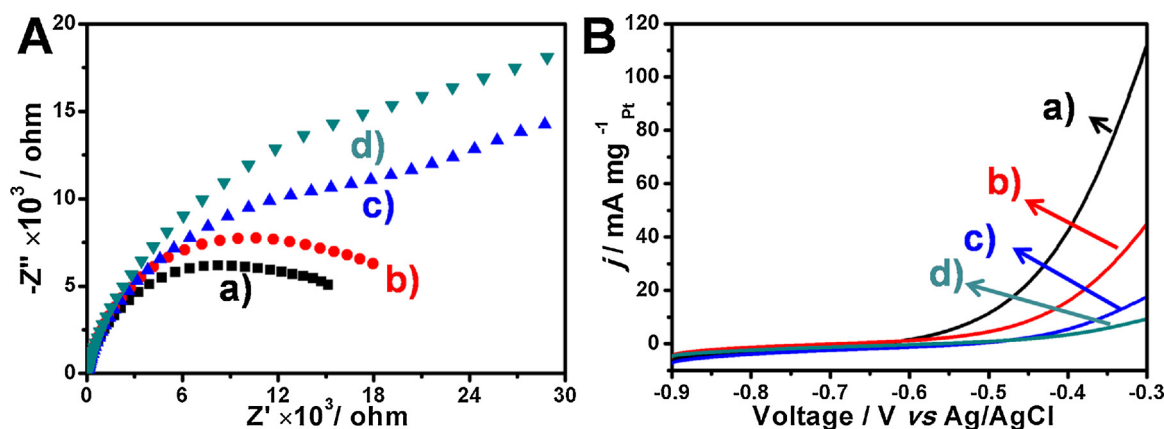
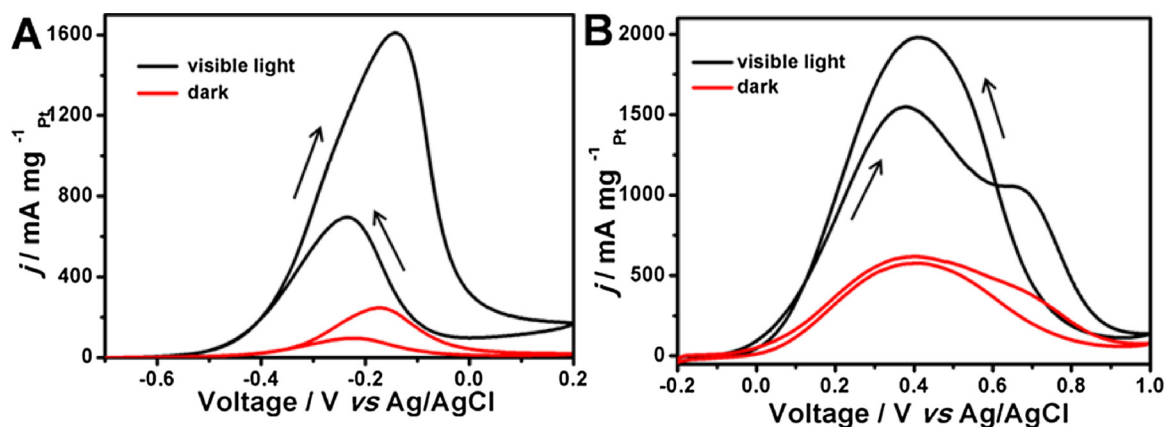


Fig. 8. The EIS (A) and LSV (B) spectra of Pt/g-C<sub>3</sub>N<sub>4</sub>/MoS<sub>2</sub> (a and b) and Pt/g-C<sub>3</sub>N<sub>4</sub> (c and d) in 1 M EtOH + 1 M KOH under visible light illumination (a and c) and dark condition (b and d).





**Fig. 9.** CVs of Pt-C<sub>3</sub>N<sub>4</sub>/MoS<sub>2</sub> electrode in 1 M MeOH + 1 M KOH solution (A) and 0.5 M HCOOH + 0.5 M H<sub>2</sub>SO<sub>4</sub> (B) under visible light illumination and dark condition.

abundant coupling interfacial sites and relative larger surface area, which facilitates migration of the photoinduced charges more easily, thereby resulting in higher photocatalytic performance.

To confirm superior charge separation in the 2D/2D composites of g-C<sub>3</sub>N<sub>4</sub>/MoS<sub>2</sub> compare to pure g-C<sub>3</sub>N<sub>4</sub>, the photocurrent response together with EIS spectra of both electrodes were evaluated in Na<sub>2</sub>SO<sub>4</sub> electrolyte. Fig. 12A shows *I*-*t* curves on the g-C<sub>3</sub>N<sub>4</sub> and g-C<sub>3</sub>N<sub>4</sub>/MoS<sub>2</sub>. When the working electrodes were under visible light irradiation, both electrodes showed rapid responsive photocurrents. However, compare to the pure g-C<sub>3</sub>N<sub>4</sub> (0.11  $\mu\text{A cm}^{-2}$ ), the 2D/2D g-C<sub>3</sub>N<sub>4</sub>/MoS<sub>2</sub> composites show 6 times enhanced photocurrent intensity (0.60  $\mu\text{A cm}^{-2}$ ). Moreover, the photocurrent responses are repeatable during on/off cycles under visible light irradiation. Furthermore, the EIS measurements

showed that the g-C<sub>3</sub>N<sub>4</sub>/MoS<sub>2</sub> under visible light illumination displays the smallest DSA than that of under dark environment and g-C<sub>3</sub>N<sub>4</sub> under light irradiation and dark environment (Fig. 12B). These results clearly confirm that light irradiation promotes the electrons mobility at the surface of electrode in g-C<sub>3</sub>N<sub>4</sub>/MoS<sub>2</sub> composites.

Photoluminescence (PL) quenching is often observed due to the altered charge migration processes in the composites. The PL emission spectra together with time-resolved fluorescence decays of pure g-C<sub>3</sub>N<sub>4</sub> and g-C<sub>3</sub>N<sub>4</sub>/MoS<sub>2</sub> nanocomposites were studied. As show in Fig. 13A, when the samples were excited at 405 nm, the PL emission of g-C<sub>3</sub>N<sub>4</sub> showed a broad peak centered at 460 nm, which matches its bandgap (ca. 2.7 eV). In the composites of g-C<sub>3</sub>N<sub>4</sub>/MoS<sub>2</sub>, PL emission intensity quenching with 61.1% was detected compare to pure g-C<sub>3</sub>N<sub>4</sub>. The

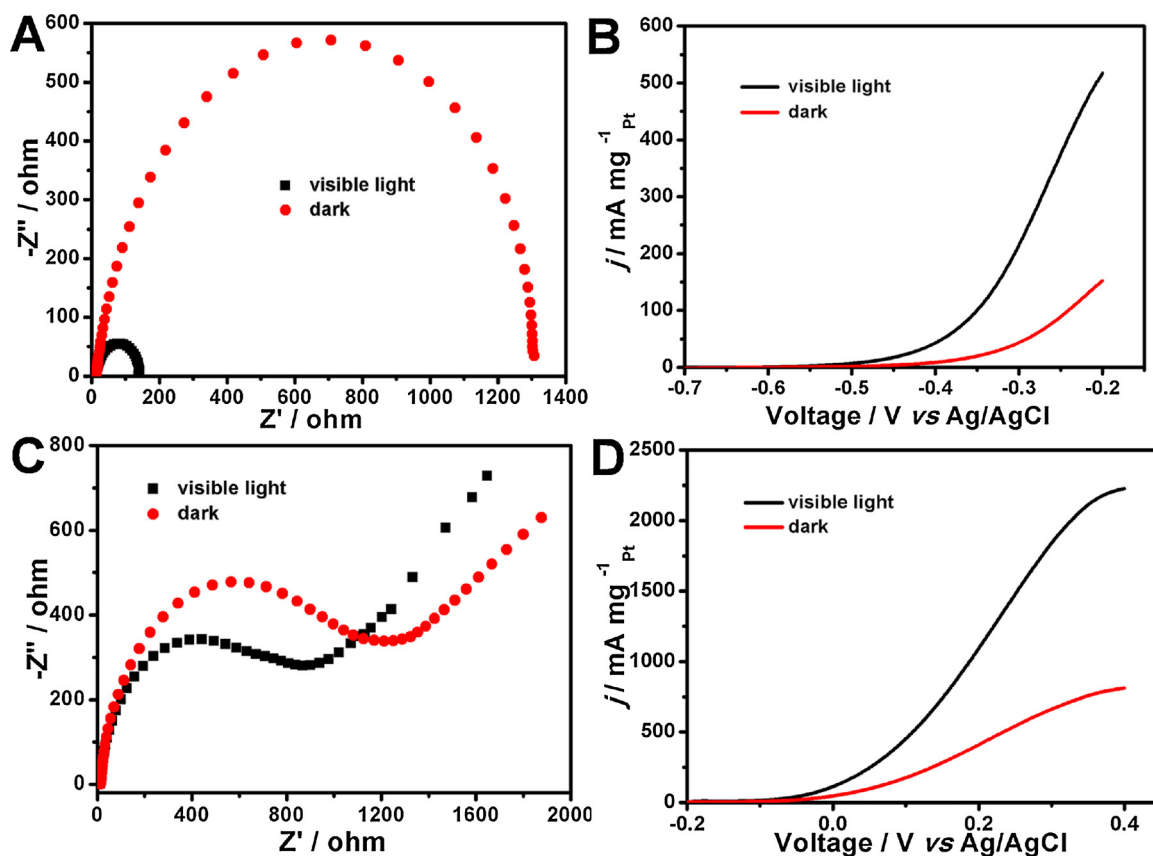


**Fig. 10.** The EIS (A and C) and LSV (B and D) spectra of Pt/g-C<sub>3</sub>N<sub>4</sub>/MoS<sub>2</sub> under visible light illumination and dark environment in 1 M MeOH + 1 M KOH (A and B) and 0.5 M HCOOH + 0.5 M H<sub>2</sub>SO<sub>4</sub> (C and D).



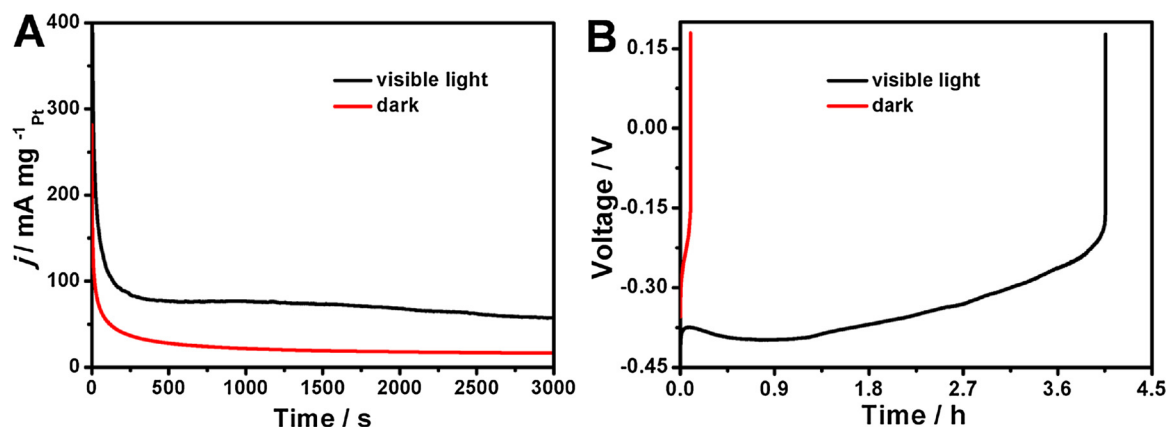


Fig. 11. Chronoamperometry (CA) at -0.2 V (A) and chronopotentiometry (CP) at 100  $\mu$ A (B) of the Pt/g-C<sub>3</sub>N<sub>4</sub>/MoS<sub>2</sub> in 1 M MeOH + 1 M KOH condition under visible light illumination and dark environment.

efficient PL quenching means much less electron-hole recombination in g-C<sub>3</sub>N<sub>4</sub>/MoS<sub>2</sub> composites, indicating the photogenerated electrons from excited g-C<sub>3</sub>N<sub>4</sub> were efficiently trapped by MoS<sub>2</sub> [11].

To probe the kinetics of electron transfer from the excited g-C<sub>3</sub>N<sub>4</sub> to MoS<sub>2</sub>, time-resolved fluorescence decay were studied, as shown in Fig. 13B and the corresponding fitted fluorescence decay data are summarized in Table 2. Pure g-C<sub>3</sub>N<sub>4</sub> shows an average lifetime ( $\tau$ ) of 1.74 ns. In the composites of g-C<sub>3</sub>N<sub>4</sub>/MoS<sub>2</sub>, the average lifetime turns to shorter. The rate of electron transfer process is calculated according Eq. (2) [51] and listed in Table 2.

$$k_{ET} = \frac{1}{\tau_{g-C_3N_4/MoS_2}} - \frac{1}{\tau_{g-C_3N_4}} \quad (2)$$

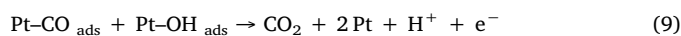
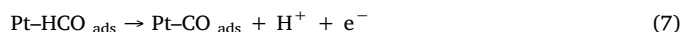
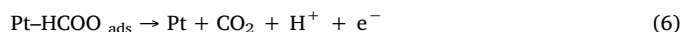
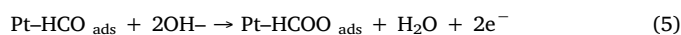
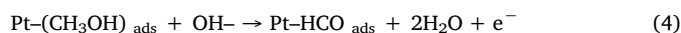
where,  $k_{ET}$  is the rate of electron transfer,  $\tau_{g-C_3N_4/MoS_2}$  is the average lifetime of excited g-C<sub>3</sub>N<sub>4</sub>/MoS<sub>2</sub>, and  $\tau_{g-C_3N_4}$  is the average lifetime of excited g-C<sub>3</sub>N<sub>4</sub>. The calculated  $k_{ET}$  is ca.  $2.8 \times 10^8$  s. This rapid electron transfer rate visually reveals an efficient electron transfer between the excited g-C<sub>3</sub>N<sub>4</sub> and the MoS<sub>2</sub> in the composites under visible light illumination, resulting in a suppressed electron-hole recombination and thereby increased photoelectrocatalytic performance.

### 3.8. Proposed mechanism of photo-enhanced electrocatalytic small organic molecules oxidation on Pt/g-C<sub>3</sub>N<sub>4</sub>/MoS<sub>2</sub> catalyst

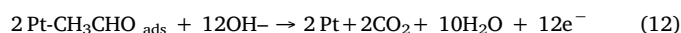
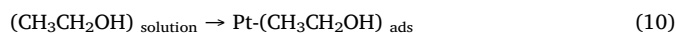
According to above results, a proposed mechanism for distinctly enhanced photoelectrocatalytic oxidation of SOMs including ethanol, methanol, and formic acid by using 2D/2D composites of Pt/g-C<sub>3</sub>N<sub>4</sub>/MoS<sub>2</sub> modified electrode was seen in Scheme 1. Firstly, in the electrocatalytic process, Pt nanoparticles deposited on the surface of g-C<sub>3</sub>N<sub>4</sub>/MoS<sub>2</sub> were acted as active sites, in which the target molecules are electro-oxidized to CO<sub>2</sub> on its surface. The main steps for the oxidation

of methanol, ethanol, and formic acid were described as follow equations:

(1) electrocatalytic oxidation of methanol [52–54]:

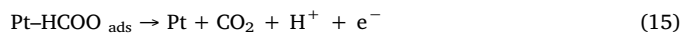
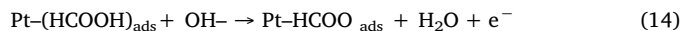


(2) electrocatalytic oxidation of ethanol: [52,55,56]



(3) electrocatalytic oxidation of formic acid: [52,57,58]

Direct oxidation processes:



Indirect oxidation processes:

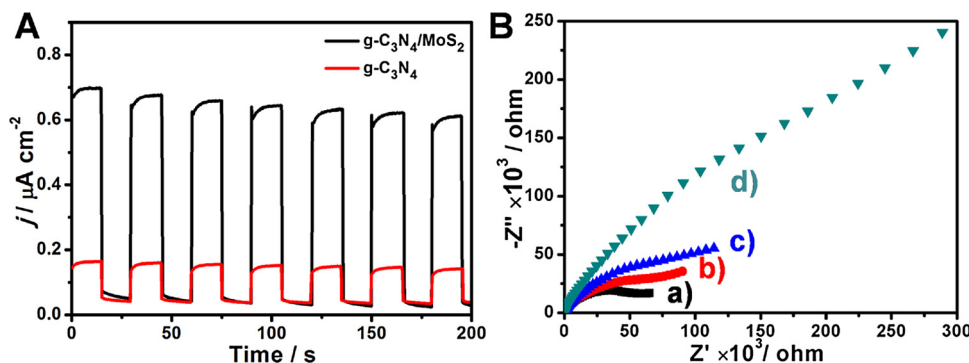
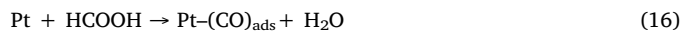


Fig. 12. Photocurrent responses (A) and EIS spectra (B) of g-C<sub>3</sub>N<sub>4</sub>/MoS<sub>2</sub> (a and b) and g-C<sub>3</sub>N<sub>4</sub> (c and d) in 0.1 M Na<sub>2</sub>SO<sub>4</sub> media at a potential of 0.6 V. The illumination was interrupted every 15 s in the photocurrent responses.

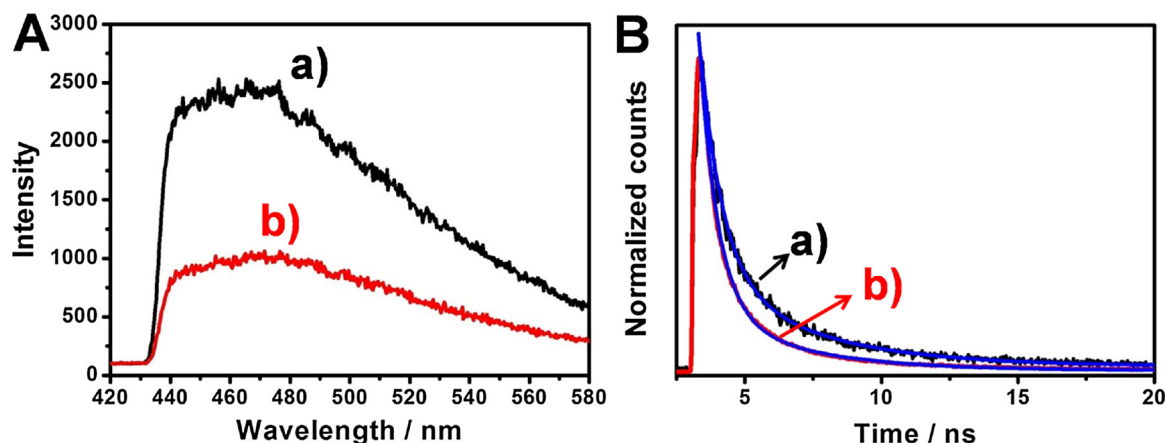
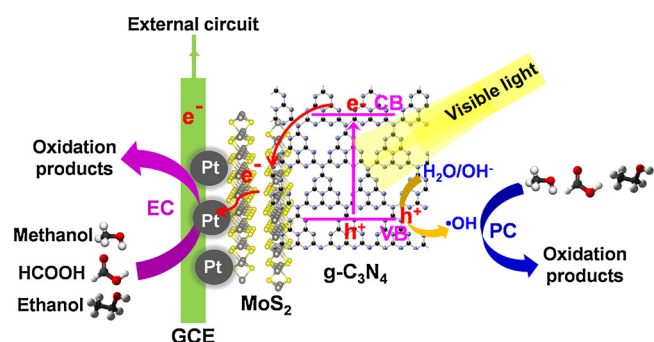


Fig. 13. PL emission spectra (A) and decay profiles (B) of the  $g\text{-C}_3\text{N}_4$  (a) and  $g\text{-C}_3\text{N}_4/\text{MoS}_2$  nanocomposites (b). Excitation wavelength: 405 nm.

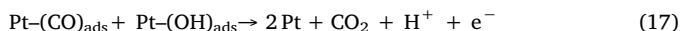
Table 2

Time-resolved PL decay data of  $g\text{-C}_3\text{N}_4$  and  $g\text{-C}_3\text{N}_4/\text{MoS}_2$  derived from Fig. 13B.

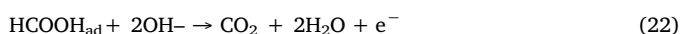
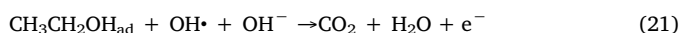
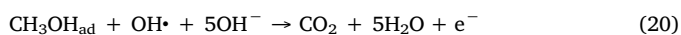
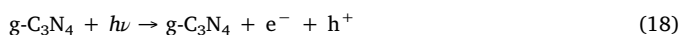
Sample	$\tau_1$ (ns)	$\tau_2$ (ns)	$\tau_{\text{ave}}$ (ns)	$k_{\text{ET}}$ ( $\text{s}^{-1}$ )
$g\text{-C}_3\text{N}_4$	0.88 (73.5%)	4.12 (26.5%)	1.74	–
$g\text{-C}_3\text{N}_4/\text{MoS}_2$	0.67 (81.4%)	3.35 (18.6%)	1.17	$2.8 \times 10^8$



Scheme 1. Proposed scheme of the electrocatalytic (EC) and photocatalytic (PC) oxidation of small organic molecules through the Pt/ $g\text{-C}_3\text{N}_4/\text{MoS}_2$  electrode under visible-light illumination.



Secondly, after Pt/ $g\text{-C}_3\text{N}_4/\text{MoS}_2$  electrode was upon visible light illumination, the photogenerated electrons and holes were formed in the conduction band (CB) and valence band (VB) of  $g\text{-C}_3\text{N}_4$ , respectively [20–23]. The surface adsorbed  $\text{OH}^-/\text{H}_2\text{O}$  was oxidized by holes to form hydroxyl radicals ( $\cdot\text{OH}$ ) [11–14,47]. Then, the SOMs and intermediate carbonaceous species which adsorbed on the surface of electrocatalyst were oxidized by formed  $\cdot\text{OH}$ s, leading to a photo-assisted catalytic process. This photocatalytic cleaning process for the removal of intermediate carbonaceous species promotes the poisoning suppression of catalysts, although the catalysts still need to bear the intermediate carbonaceous species after long time catalytic process. The corresponding steps are showing as follows: [59–61]



In the pure  $g\text{-C}_3\text{N}_4$ , these electron-hole pairs are recombined easily and only a small fraction of holes can be used for photocatalytic cleavage. However, in the presence of  $\text{MoS}_2$ , owing to the effective electrons transfer between  $g\text{-C}_3\text{N}_4$  and  $\text{MoS}_2$  [26–30], the electrons are easily injected to  $\text{MoS}_2$  and then flow to Pt and electrode by external electric field, thereby limiting the charges recombination and improving the catalytic performance and stability.

To confirm the hydroxyl radicals ( $\cdot\text{OH}$ ) were generated in the samples of  $g\text{-C}_3\text{N}_4$  and  $g\text{-C}_3\text{N}_4/\text{MoS}_2$  during visible light illumination, electron spin resonance (ESR) spectroscopy was investigated. We used 5,5-dimethyl-1-pyrroline *N*-oxide (DMPO) as spin trapping adducts to detect the formation of  $\cdot\text{OH}$ . Fig. 14 shows four-line spectra with relative intensities of 1:2:2:1 in the system of  $g\text{-C}_3\text{N}_4$  after visible light illumination, indicating that the  $\cdot\text{OH}$  can be generated in the presence of  $g\text{-C}_3\text{N}_4$  under visible light illumination [62]. Moreover, after hybridization of  $\text{MoS}_2$ , the signals of  $\cdot\text{OH}$ s were improved obviously. This phenomenon further confirms that the electrons from excited  $g\text{-C}_3\text{N}_4$  were rapidly transport to  $\text{MoS}_2$ , resulting in an effective charge separation and enhanced the catalytic performance.

#### 4. Conclusions

In summary, 2D/2D heterostructure of  $g\text{-C}_3\text{N}_4/\text{MoS}_2$  nanocomposite was synthesized to be a photofunctional support for Pt nanoparticles decoration. The as-prepared Pt/ $g\text{-C}_3\text{N}_4/\text{MoS}_2$  exhibited efficient catalytic activities towards the oxidation of SOMs including ethanol,

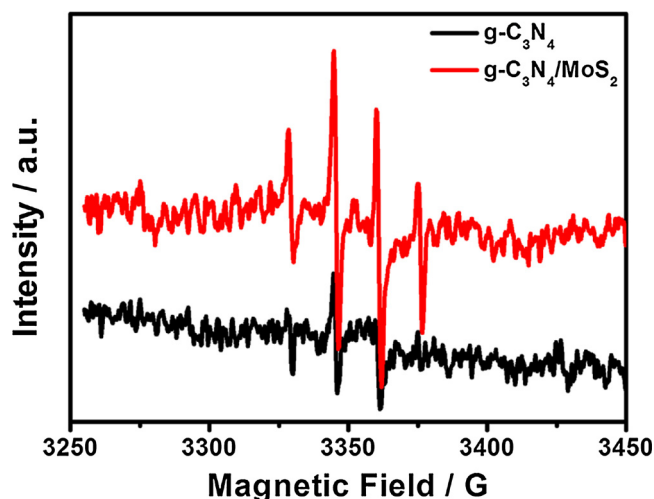


Fig. 14. ESR spectra of DMPO- $\cdot\text{OH}$  adducts in the system of  $g\text{-C}_3\text{N}_4$  and  $g\text{-C}_3\text{N}_4/\text{MoS}_2$ .

methanol, and formic acid. Furthermore, with the assistance of visible light illumination, the performance was distinctly improved owing to the synergistic effect of electro- and photo-process. By coupling MoS<sub>2</sub> nanosheets on the surface of the g-C<sub>3</sub>N<sub>4</sub>, the effective charge separation in the designed 2D/2D heterostructure of g-C<sub>3</sub>N<sub>4</sub>/MoS<sub>2</sub> contributes to the higher catalytic performance compared to single-component of g-C<sub>3</sub>N<sub>4</sub> upon visible light irradiation. The present results suggest that the 2D/2D heterostructure of g-C<sub>3</sub>N<sub>4</sub>/MoS<sub>2</sub> are a promising photo-functional substrate in the fields of chemical and solar energy conversion.

## Acknowledgments

Research was supported by the National Natural Science Foundation of China (41522304, 21577142, 21603111, and 51702173) and also supported by K.C. Wong Magna Fund in Ningbo University.

## Appendix A. Supplementary data

Supplementary material related to this article can be found, in the online version, at doi:<https://doi.org/10.1016/j.apcatb.2018.10.047>.

## References

- [1] C. Bianchini, P. Kang Shen, *Chem. Rev.* 109 (2009) 4183–4206.
- [2] F. Vigier, S. Rousseau, C. Coutanceau, J.-M. Leger, C. Lamy, *Top. Catal.* 40 (2006) 111–121.
- [3] C. Rice, S. Ha, R.I. Masel, A. Wieckowski, *J. Power Sources* 115 (2003) 229–235.
- [4] E. Antolini, *J. Power Sources* 170 (2007) 1–12.
- [5] M. Cao, D.S. Wu, R. Cao, *ChemCatChem* 6 (2014) 26–45.
- [6] M. Zhu, C. Zhai, C. Lu, *Advanced Electrode Materials*, Ch.11 John Wiley & Sons, Inc., Hoboken, NJ, USA, 2016, pp. 435–456.
- [7] S. Sfaelou, P. Lianos, *AIMS Mater. Sci.* 3 (2016) 270–288.
- [8] K. Drew, G. Girishkumar, K. Vinodgopal, P.V. Kamat, *J. Phys. Chem. B* 109 (2005) 11851–11857.
- [9] M. Sun, J. Hu, C. Zhai, M. Zhu, J. Pan, *Electrochim. Acta* 245 (2017) 863–871.
- [10] C. Zhai, M. Zhu, F. Pang, D. Bin, C. Lu, M.C. Goh, P. Yang, Y. Du, *ACS Appl. Mater. Interfaces* 8 (2016) 5972–5980.
- [11] C. Zhai, M. Sun, M. Zhu, K. Zhang, Y. Du, *Int. J. Hydrogen Energy* 42 (2017) 5006–5015.
- [12] A. Leelavathi, G. Madras, N. Ravishanker, *J. Am. Chem. Soc.* 136 (2014) 14445–14455.
- [13] A. Arabzadeh, A. Salimi, M. Ashrafi, S. Soltanian, P. Servati, *Catal. Sci. Technol.* (6) (2016) 3485–3496.
- [14] J.A. Díaz-Real, E. Ortiz-Ortega, M.P. Gurrola, J. Ledesma-Garcia, L.G. Arriaga, *Electrochim. Acta* 206 (2016) 388–399.
- [15] Y.-H. Hsu, A.T. Nguyen, Y.-H. Chiu, J.-M. Li, Y.-J. Hsu, *Appl. Catal. B Environ.* 185 (2016) 133–140.
- [16] C. Zhai, M. Zhu, D. Bin, H. Wang, Y. Du, C. Wang, P. Yang, *ACS Appl. Mater. Interfaces* 6 (2014) 17753–17761.
- [17] K.S. Novoselov, A. Mishchenko, A. Carvalho, A.H. Castro Neto, *Science* 353 (2016) 1–11.
- [18] M.-Y. Li, C.-H. Chen, Y.M. Shi, L.-J. Li, *Mater. Today* 19 (2016) 322–335.
- [19] W.-J. Ong, *Front. Mater.* 4 (2017) 11.
- [20] W. Jiang, W. Luo, J. Wang, M. Zhang, Y. Zhu, *J. Photochem. Photobiol. C* 28 (2016) 87–115.
- [21] J.Q. Wen, J. Xie, X.B. Chen, X. Li, *Appl. Surf. Sci.* 391 (2017) 72–123.
- [22] J.S. Zhang, Y. Chen, X.C. Wang, *Energy Environ. Sci.* 8 (2015) 3092–3108.
- [23] Y. Zheng, L.H. Lin, B. Wang, X.C. Wang, *Angew. Chem. Int. Ed.* 54 (2015) 12868–12884.
- [24] G.G. Zhang, Z.-A. Lan, X.C. Wang, *Angew. Chem. Int. Ed.* 55 (2016) 15712–15727.
- [25] Y.D. Hou, A.B. Laursen, J.S. Zhang, G.G. Zhang, Y.S. Zhu, X.C. Wang, S. Dahl, I. Chorkendorff, *Angew. Chem. Int. Ed.* 52 (2013) 3621–3625.
- [26] J.J. Wang, Z.Y. Guan, J. Huang, Q.X. Li, J.L. Yang, *J. Mater. Chem. A* 2 (2014) 7960–7966.
- [27] J. Yan, Z.G. Chen, H.Y. Ji, Z. Liu, X. Wang, Y.G. Xu, X.J. She, L.Y. Huang, L. Xu, H. Xu, H.M. Li, *Chem. Eur. J.* 22 (2016) 4764–4773.
- [28] Q. Li, N. Zhang, Y. Yang, G.Z. Wang, D.H.L. Ng, *Langmuir* 30 (2014) 8965–8972.
- [29] J. Li, E.Z. Liu, Y.N. Ma, X.Y. Hu, J. Wan, L. Sun, J. Fan, *Appl. Surf. Sci.* 364 (2016) 694–702.
- [30] H. Zhao, Y.M. Dong, P.P. Jiang, H.Y. Miao, G.L. Wang, J.J. Zhang, *J. Mater. Chem. A* 3 (2015) 7375–7381.
- [31] Z.Y. Zhang, D.L. Jiang, D. Li, M.Q. He, M. Chen, *Appl. Catal. B Environ.* 183 (2016) 113–123.
- [32] C.L. Tan, H. Zhang, *Chem. Soc. Rev.* 44 (2015) 2713–2731.
- [33] X. Li, H.W. Zhu, *J. Mater. Sci.* 1 (2015) 33–44.
- [34] K. Chang, X. Hai, J.H. Ye, *Adv. Energy Mater.* 6 (2016) 1–21.
- [35] K. Pramoda, U. Gupta, M. Chhetri, A. Bandyopadhyay, S.K. Pati, C.N.R. Rao, *ACS Appl. Mater. Interfaces* 9 (2017) 10664–10672.
- [36] J. Li, E.Z. Liu, Y.N. Ma, X.Y. Hu, J. Wan, L. Sun, J. Fan, *Appl. Surf. Sci.* 364 (2016) 694–702.
- [37] X.J. Lu, Y.L. Jin, X.Y. Zhang, G.Q. Xu, D.M. Wang, J. Lv, Z.X. Zheng, Y.C. Wu, *Dalton Trans.* 45 (2016) 15406–15414.
- [38] S.A. Ansari, M.H. Cho, *Sci. Rep.* 7 (2017) 1–11.
- [39] X. Shi, M. Fujitsuka, S. Kim, T. Majima, *Small* 14 (2018) 1–9.
- [40] M.S. Zhu, C.Y. Zhai, M.J. Sun, Y.F. Hu, B. Yan, Y.K. Du, *Appl. Catal. B Environ.* 203 (2017) 108–115.
- [41] Z.Y. Zhang, K.C. Liu, Z.Q. Feng, Y.N. Bao, B. Dong, *Sci. Rep.* 6 (2016) 1–10.
- [42] C. Zhai, M. Zhu, D. Bin, F. Ren, C. Wang, P. Yang, Y. Du, *J. Power Sources* 275 (2015) 483–488.
- [43] M. Zhu, Z. Li, Y. Du, Z. Mou, P. Yang, *ChemCatChem* 4 (2012) 112–117.
- [44] C. Wang, H. Wang, C. Zhai, F. Ren, M. Zhu, P. Yang, Y. Du, *J. Mater. Chem. A* 3 (2015) 4389–4398.
- [45] Z. Yao, R. Yue, F. Jiang, C. Zhai, F. Ren, Y. Du, *J. Solid State Electrochem.* 17 (2013) 2511–2519.
- [46] M. Sun, J. Hu, C. Zhai, M. Zhu, J. Pan, *ACS Appl. Mater. Interfaces* 9 (2017) 13223–13230.
- [47] F. Liang, Y. Zhu, *Appl. Catal. B* 180 (2016) 324–329.
- [48] M. Zhu, Y. Osakada, S. Kim, M. Fujitsuka, T. Majima, *Appl. Catal. B Environ.* 217 (2017) 285–292.
- [49] M. Zhu, X. Cai, M. Fujitsuka, J. Zhang, T. Majima, *Angew. Chem. Int. Ed.* 56 (2017) 2064–2068.
- [50] F. Ren, H. Wang, C. Zhai, M. Zhu, R. Yue, Y. Du, P. Yang, J. Xu, W. Lu, *ACS Appl. Mater. Interfaces* 6 (2014) 3607–3614.
- [51] M. Zhu, Y. Dong, Y. Du, Z. Mou, J. Liu, P. Yang, X. Wang, *Chem. Eur. J.* 18 (2012) 4367–4374.
- [52] M.H. Shao, *Electrocatalysis in Fuel Cells: A non- and Low- Platinum Approach*, Springer, London, 2013.
- [53] R. Nagao, D.A. Cantane, F.H.B. Lima, H. Varela, *Phys. Chem. Chem. Phys.* 14 (2012) 8294–8298.
- [54] Y.X. Chen, A. Miki, S. Ye, H. Sakai, M. Osawa, *J. Am. Chem. Soc.* 125 (2003) 3680–3681.
- [55] E. Antolini, *Energies* 10 (2017) 1–20.
- [56] M.A.F. Akhairi, S.K. Kamarudin, *Int. J. Hydrogen Energy* 41 (2016) 4214–4228.
- [57] M.G. Hosseini, M.M. Momeni, *Fuel Cells* 3 (2012) 406–414.
- [58] N. Mojmudar, S. Sarker, S.A. Abbas, Z. Tian, V. Subramanian, *ACS Appl. Mater. Interfaces* 6 (2014) 5585–5594.
- [59] A.Y. Ahmed, T.A. Kandiel, I. Ivanova, D. Bahnemann, *Appl. Surf. Sci.* 319 (2014) 44–49.
- [60] M. Hamandi, G. Berhault, C. Guillard, H. Kochkar, *Appl. Catal. B* 209 (2017) 203–213.
- [61] P. Panagiotopoulou, M. Antoniadou, D.I. Kondarides, P. Lianos, *Appl. Catal. B* 100 (2010) 124–132.
- [62] H.H. Ji, F. Chang, X.F. Hu, W. Qin, J.W. Shen, *Chem. Eng. J.* 218 (2013) 183–190.